Rheology of debris-flow materials is controlled by the distance from jamming

Robert Kostynick[1,2†∠], Hadis Matinpour[3†◇], Shravan Pradeep[2†§], Sarah Haber[4∨], Alban Sauret[3○], Eckart Meiburg[3∪], Thomas Dunne[5⊤], Paulo Arratia[6∩], and Douglas Jerolmack[2,6*]

[1]Washington University in St. Louis, Earth and Planetary Sciences, St. Louis, MO, United States
[2]University of Pennsylvania, Earth and Environmental Science, Philadelphia, PA, United States
[3]University of California Santa Barbara, Mechanical Engineering, Santa Barbara, CA, United States
[4]Ramboll US Consulting Inc., Princeton, NJ, United States
[5]University of California Santa Barbara, Bren School of Environmental Science and Management, Santa Barbara, CA, United States
[6]University of Pennsylvania, Mechanical Engineering and Applied Mechanics, Philadelphia, PA, United States

[*]To whom correspondence should be addressed; E-mail: sediment@sas.upenn.edu.

[†] Authors contributed equally to this paper.

[∠]kostynick.r@wustl.edu
[◇]h.matinpour@gmail.com
[§]spradeep@sas.upenn.edu
[∨]sarahjhaber@gmail.com
[○]asauret@engineering.ucsb.edu
[∪]meiburg@engineering.ucsb.edu
[⊤]tdunne@ucsb.edu
[∩]parratia@seas.upenn.edu
[*]sediment@sas.upenn.edu

Rheology of debris-flow materials is controlled by the distance from jamming

Robert Kostynick[1,2†], Hadis Matinpour[3†], Shravan Pradeep[2†], Sarah Haber[4], Alban Sauret[3], Eckart Meiburg[3], Thomas Dunne[5], Paulo Arratia[6], and Douglas Jerolmack[2,6*]

[1]Washington University in St. Louis, Earth and Planetary Sciences, St. Louis, MO, United States
[2]University of Pennsylvania, Earth and Environmental Science, Philadelphia, PA, United States
[3]University of California Santa Barbara, Mechanical Engineering, Santa Barbara, CA, United States
[4]Ramboll US Consulting Inc., Princeton, NJ, United States
[5]University of California Santa Barbara, Bren School of Environmental Science and Management, Santa Barbara, CA, United States
[6]University of Pennsylvania, Mechanical Engineering and Applied Mechanics, Philadelphia, PA, United States

*To whom correspondence should be addressed; E-mail: sediment@sas.upenn.edu.
† Authors contributed equally to this paper.

Debris flows are dense and fast-moving complex suspensions of soil and water that threaten lives and infrastructure. Assessing the hazard potential of debris flows requires predicting yield and flow behavior. Reported measurements of

rheology for debris-flow slurries are highly variable and sometimes contradictory, due to heterogeneity in grain size, shape, chemical composition, and solid-volume fraction (ϕ). Here we examine the composition and flow behavior of source materials that formed the post-wildfire debris flows in Montecito, CA in 2018, for a wide range of ϕ that encapsulates debris-flow formation by overland flow. We find that shear viscosity and yield stress are controlled by the distance from jamming, $\Delta\phi = \phi_m - \phi$, and that the jamming fraction ϕ_m depends on grain-size polydispersity and friction. By re-scaling shear and viscous stresses to account for these effects, the data collapse onto a simple non-dimensional flow curve indicative of a Bingham plastic (viscoplastic) fluid. Given the highly nonlinear dependence of rheology on $\Delta\phi$, our findings suggest that determining the jamming fraction for natural materials will significantly improve flow models for geophysical suspensions such as hyperconcentrated flows and debris flows.

Introduction

When intense rainfall soaks the soil on steep mountain hillsides, water and particulates can mix to form a dense, viscous suspension called a debris flow (*1*). Debris flows may form catastrophically, such as landslides that collapse into valley-bottom channels and mix with river water (*2*); or gradually, as overland flow on steep hillsides progressively entrains soil (*3*, *4*). Debris flows are particularly hazardous due to their high speed and density (*5*), and because their fluidity allows them to spread rapidly when flows become unconfined — for example, upon exiting a canyon (*6*). As debris flows spread they slow down and eventually "freeze", implying that a minimum shear stress (τ) is necessary to sustain flow (*7–9*). A simple rheologic model

that captures the observed phenomenology is the widely applied Herschel-Bulkley equation,

$$\tau = \tau_o + k\dot{\gamma}^n, \tag{1}$$

where τ [Pa] is the shear stress, τ_o [Pa] is the yield stress, $\dot{\gamma}$ [s^{-1}] is the shear rate, and k is an empirical coefficient with dimension that depends on the value of the exponent. The exponent n is the flow index, where in general, $n < 1$ corresponds to shear thinning and $n > 1$ is associated with shear thickening behavior.

In typical constant volume steady-shear rheology experiments, like those we present in this study, a suspension with fixed ϕ is placed in a fluid gap of thickness h and one boundary is sheared at a constant velocity u while the shear stress is measured. The resulting data are used to produce a flow curve, τ vs. $\dot{\gamma} \approx u/h$, from which the shear viscosity $\eta = \tau/\dot{\gamma}$ can be obtained. Due to its flexibility, the Herschel-Bulkley model has been applied widely to fit the flow curves of debris-flow materials (*10–12*). Parameter values, however, are inconsistent among different studies and can show extreme sensitivity to ϕ and also to material composition (clay/silt/sand content) (*8*, *10*, *13*, *14*). For example: τ_o increases rapidly with ϕ, but the functional form appears to vary among studies (*8*, *14*, *15*); and flow behavior of sand-water mixtures was found to change from highly shear thinning ($n < 0.5$) to "Bingham like" ($n \approx 1$) with the addition of small amounts of clay (*16*). While most reported debris-flow data indicate apparent shear thinning behavior ($n < 1$), some mixtures appear to exhibit shear thickening ($n > 1$) (*9*, *10*, *12*, *16–20*). Thus, the Herschel-Bulkley model provides a compact description of the flow curve for a given sample, but model results may not be extrapolated to different settings or geometries because the physical meaning of the fitting parameters is unclear (*21*). More broadly, researchers have challenged the use of a fixed rheology model like Eq. (1) for natural debris flows because it does not include feedbacks among ϕ, $\dot{\gamma}$ and pore-fluid pressure (*22–24*). More sophisticated models that incorporate these effects have shown promise for describing the

failure and runout of debris flows (*25*, *26*). Yet, these models still require constitutive relations among stress, shear rate and volume fraction.

A physically informed non-dimensionalization of the Herschel-Bulkley model was proposed by Coussot (*15*), and was shown to collapse much of the variability in flow curves of clay suspensions – a model mud system. At rest, dense athermal (non-colloidal) suspensions maintain a residual yield stress due to grain bonding (cohesion) and/or granular (Coulomb) friction (*8*, *15*, *27*). Such yield-stress materials behave elastically over a range of shear rates, exhibiting a constant stress $\tau = \tau_o$. This suggests that shear stress should be rescaled as $\tau^* = \tau/\tau_o$. Under vigorous shear (large $\dot{\gamma}$) the suspension begins to flow. The effective suspension viscosity, $\eta(\phi)$, increases with ϕ due to hydrodynamic and frictional interactions among particles (*8*, *15*, *28*). Coussot (*15*) proposed a dimensionless shear rate, $\Gamma = \eta(\phi)\dot{\gamma}/\tau_o$, that represents a ratio of the characteristic timescales of the material ($\eta(\phi)/\tau_o$) and the flow ($1/\dot{\gamma}$). Note that Γ is also the inverse of the Bingham number, which characterizes the ratio of elastic and viscous stresses; however, here the viscous stress $\eta(\phi)\dot{\gamma}$ is associated with the effective viscosity of the suspension $\eta(\phi)$, not water (*8*, *15*, *27*). The nondimensional Herschel-Bulkley relation becomes:

$$\tau^* = 1 + \Gamma^N, \tag{2}$$

where the modified flow index N may be different from the value n determined from the original Herschel-Bulkley given by Eq. (1). Equation (2) has the advantage that all model parameters are dimensionally homogeneous. Collapsing debris-flow data using this relation may also provide a more reliable estimate of the flow index, perhaps reducing the range of reported exponents and providing insights on mechanical flow behavior.

In order to apply the dimensionless Herschel-Bulkley Eq. (2) to flow data, we must determine the functional dependence of η on ϕ. One way to think about the initiation and cessation of flows of dense suspensions is as a jamming transition (*29*) — that is, a continuous transi-

tion between rigid and flowing states where flow is arrested in the direction of applied shear at a "jamming fraction" $\phi = \phi_m$ (*28*, *30*). The parameter ϕ_m for suspensions is analogous to the critical-state volume fraction in soil mechanics (*31*). In this framework, suspension viscosity is primarily controlled by the distance from jamming, $\Delta\phi = \phi_m - \phi$. As particles are added to a fluid, the effective viscosity increases; first from drag and hydrodynamic interactions among particles, and eventually (as $\phi \rightarrow \phi_m$) due to geometric confinement and friction among the grains (*30*). Boyer *et al.* (*28*) presented a model for athermal suspensions that effectively captures the observed dependence of η on ϕ, and also ϕ-dependent granular contact friction μ^c:

$$\eta(\phi)/\eta_f = 1 + 5/2 \cdot \phi\Big(1 - \phi/\phi_m\Big)^{-1} + \mu^c(\phi)\Big(\phi/\Delta\phi\Big)^2 \tag{3}$$

where η_f is the viscosity of the suspending fluid. The parameter ϕ_m depends on material properties: increased surface roughness decreases ϕ_m (*32*, *33*), whereas increased grain-size polydispersity increases ϕ_m by allowing higher packing densities (*34*). Equation (3) has important implications for understanding the mobility of geophysical flows across a range of ϕ; from hyperconcentrated flows having intermediate sediment concentrations (*35*) to high-concentration debris-flows. In the dilute regime ($\phi << \phi_m$), the third term in Eq. (3) that represents granular interactions is negligible, and viscosity increases linearly with ϕ. For dense suspensions corresponding to small $\Delta\phi$, however, the third term is dominant. Since the empirical friction parameter μ^c varies only by a factor ~ 2 over the entire range of ϕ (*28*), the viscosity of dense suspensions scales as $\eta(\phi) \propto (\Delta\phi)^{-2}$. For suspensions close to the jamming limit, changing ϕ or ϕ_m by even 1% can change the effective viscosity by orders of magnitude. Yet, debris-flow models typically set a constant ϕ_m for simplicity (*15*, *26*, *31*).

In this study we examine soil sampled from the source areas of the 2018 debris flows that occurred in the Santa Ynez Mountains in Montecito, California (USA), a devastating event that resulted in 23 fatalities and 408 damaged homes (*4*). Previous field studies have constrained

the timing, generation, runout and damage associated with the debris flows (*4*, *5*). A simulation study of the Montecito debris flows examined the sensitivity of existing numerical models to constitutive equations and the value of ϕ_m (*26*). The goals of this study are to test the applicability of Equations (2) and (3) for describing the rheologic behavior of suspensions of natural soils, and to relate model parameters to the physical and chemical composition of particulates. Application of Eq. (2) to debris-flow curves would require experimental determination of three parameters: ϕ_m, μ^c and τ_o. We anticipate also that $\tau_o = f(\Delta\phi)$, since yielding occurs via breaking of grain contacts (*15*, *27*), but the functional dependence is unclear from existing data in the literature. We conduct an exhaustive laboratory examination of the steady-shear flow behavior of hillslope soils, when mixed with water over a wide range of ϕ values – from dilute to nearly jammed. We find striking confirmation of Eq. (3) from these data, despite the wide heterogeneity in grain size and mineralogy of the natural soils. Moreover, we demonstrate that ϕ_m varies systematically with grain-size polydispersity and friction. Data confirm that yield stress varies predominantly with the distance from jamming $\Delta\phi$, while the control of measured chemical composition is ambiguous. Our flow-curve measurements are well described by Eq. (2) with a fixed exponent of $N = 1$, which provides a compact constitutive equation that accounts for shear-rate and volume-fraction effects. These results clarify the distinct material controls on the rheology of debris-flow slurries, reconcile disparate observations and models, and provide a protocol for practitioners to determine the relevant parameters in a straightforward manner.

Results

Field estimates of debris-flow properties

In December of 2017, a large wildfire occurred on the steep hillslopes of the Santa Ynez mountains north of Montecito, California (USA). Vegetation was almost completely incinerated to soil depths of 3-5 cm; root mass and humic carbonaceous materials were removed. The average

bulk density of this burned topsoil was 1400 kg/m^3, whereas the unburned subsoil retained its sparser roots and an average bulk density of 1700 kg/m^3 (*4*). Assuming a grain density of 2700 kg/m^3, this indicates that burned topsoil had an average soil volume fraction of $\phi = 0.52$ while unburned subsoil had an average value of $\phi = 0.63$. Three weeks later, intense rainfall over a $10-15$ minute period resulted in concentrated hillside erosion in the form of a dense network of rills (*4*). As rainwater flowed down slopes $> 35^o$, it progressively entrained soil and increased ϕ to create fully-formed debris flows – with yield-stress features such as levees and lobes – over distances of approximately 100 m (Fig. 1). Using rainfall-runoff modeling and lidar topography data, a recent study estimated an average volume fraction of $\phi = 0.51$ for debris-flow slurries issuing from hillslope rills across the area (*4*). This same study indicated that burned surface soils maintained some degree of cohesion, inferring an effective cohesive stress on the order 10^2 Pa.

The hillslope-generated debris flows, containing particles ranging in size from clay ($\sim$ 20 μm) to gravel ($\sim$ 1mm), accumulated in valley-bottom channels where they entrained boulders up to $\sim$ 6 m in diameter (*5*, *36*). As the debris flows exited the canyons and progressed down fans, they spread outwards from the channel leaving deposits (Fig. 1a). Because sediments entrained from the valley bottoms by the debris flows contained very little sand or finer sediment, grain-size distributions from fan deposits were similar to those of soils sampled from hillslope source areas (*5*). Thus, mechanical behavior inferred from the downstream flows and their deposits help to constrain the nature of debris flows generated on hillslopes. The shear stress of debris flows observed downstream of the canyon outlets can be estimated as $\tau = \rho g H S$ while shear rate is roughly $\dot{\gamma} = u/H$, where $\rho = 2000$ kg/m^3 is the assumed suspension density and g is gravity. Using representative values for flow depth $H = 2$ m, surface slope $S = 0.04$, and flow speed $u = 4$ m/s (*5*, *26*), we estimate τ = 1600 Pa and $\dot{\gamma} = 2$ s^{-1}. We observed "frozen" deposits with depths of roughly 20 cm, from which we infer a yield stress of roughly τ_o =200

Pa. The flow viscosity can be estimated as $\eta = \tau/\dot{\gamma} = 800$ Pa.s. While these estimates are crude, τ_o of order 10^2 Pa and η of order 10^2 Pa.s are consistent with expectations for high-ϕ debris flows (*10*, *37–39*).

Composition of source materials

Over the two months following the event, we sampled burned topsoils (down to 5 cm depth) and unburned subsoils (5-20 cm depth) from inter-rill areas on hillslopes in two watersheds within the Santa Ynez mountains that served as source materials (see Supplementary Table S.1) for the debris flows (Fig. 1). Our sampling strategy was designed to examine potential controls of lithology, burning, and position within the watershed on the composition and rheology of soils (Supplementary Text S1). Despite significant variation among samples, however, we found no systematic change in soil composition due to any of these factors (Fig. S1; Supplementary Table S.2). The soils were sieved to remove particles $> 500\,\mu$m in order to prevent clogging of grains in the thin gap of the rheometer. Although removing larger grains may influence the mechanical properties of soil slurries, the volume fraction removed was $< 5\%$ for all samples.

Sonication was applied to aqueous suspensions of the soils in order to break up aggregates, and grain size was measured using a laser diffraction device (Methods). All soil samples contained particles ranging from clay to coarse sand, had a mean grain size in the very-fine sand range ($60 - 120\,\mu$m), and displayed significant peaks in the fine silt (20-30 μm) and fine sand ($\sim 200\,\mu$m) ranges (Fig. 2; Supplementary Table S.2). The biggest difference among samples was the fraction of particles larger than fine sand ($> 250\,\mu$m; Fig. 2). For comparison to other studies, we approximate polydispersity by fitting a log-normal distribution to the data and computing m_3/m_2^2, where $m_k \equiv M_k/{M_1}^k$ and M_k is the k-th moment of the distribution (*40*). Extrapolating results from simulations of idealized spheres (*40*, *41*), we anticipate that the factor ~ 3 range in polydispersity values may give rise to variation in the jamming fraction of

roughly 10% among the samples; however, we know of no studies that have examined ϕ_m for suspensions with such large polydispersity values as our soils.

We performed semi-quantitative X-Ray Diffraction (XRD) measurements to infer the bulk mineralogy of soils (see Methods). This technique has several important limitations: it can only detect crystalline phases, so any amorphous materials are unmeasured; and minerals with similar crystal structure, such as some micas and clays, cannot be easily separated. All samples were composed of three main components of interest: silica, micas such as muscovite, and clays including illite and kaolinite (Fig. S1). We were unable to differentiate some minerals such as muscovite and illite, so we examine the fraction of micas + clays as a proxy for bulk clay content (see Supplementary Text S3). This fraction varied by a factor of two across the samples; given the highly nonlinear dependence of yield stress on clay content (*8*, *14*, *15*), we expect a significant effect of cohesion on rheology for these natural soils.

Rheology of soil suspensions

We used a parallel-plate rheometer with the following specifications: the top plate diameter of 4 mm, a gap of h=1 mm, sample volume of 5 mL, and a shear-rate range of 0.01 $s^{-1} \leq \dot{\gamma} \leq 100$ s^{-1}. The small gap size is used to ensure that the suspensions are homogeneously mixed across the sample during shear, which is especially important for heavy grains that may sediment during shear in larger systems. The particle pressure associated with sedimentation sets a minimum scale for reliable stress estimates, as lower stresses may be insufficient to keep grains in suspension; for our materials this corresponds to $\tau \sim 10^{-1}$ Pa (Methods). For this study we are interested in comparing steady-shear behavior, so we adopted a shear protocol designed to minimize transient effects and hysteresis (*42*): samples were pre-sheared at the highest rate ($\dot{\gamma}$ = 100 s^{-1}) to break up aggregates, and then $\dot{\gamma}$ was ramped down in steps to the minimum value and back up. We averaged shear stress values at each step (see Methods)

to produce flow curves (τ vs. $\dot{\gamma}$) for each suspension. For a given soil sample, we prepared suspensions at several volume fractions in the range $0.05 \leq \phi \leq 0.50$ by mixing particulates with deionized water. The highest achievable ϕ is limited by instrument errors that occur as material jams. In connecting these rheometer measurements to the formation of debris flows on the hillslopes, one can envision suspensions with increasing ϕ as representing snapshots along the hillslope profile from ridge to valley. In this manner, the rheometer measurements may inform the evolution in flow behavior as water progressively entrained soil downslope.

Flow curves for all samples confirm that as ϕ is raised, shear stress and viscosity increase and the suspensions develop a yield stress — evident as a near-constant τ at low $\dot{\gamma}$ (Fig. 3). All flow curves can be closely fit with the Herschel-Bulkley model (Eq. 1) which allows estimation of yield stress (τ_0) and flow index (n). The lower limit for reliable estimates of yield stress is $\tau_o = 0.1$ Pa (see Methods), and the highest observed values reach $\tau_o \approx 200$ Pa. Most suspensions with $\phi \geq 0.2$ appear to be shear thinning ($n < 1$); however, values for n vary widely from 0.37 up to 1.45. Based on the discussion above, we suspect this is because the effects of ϕ, cohesion and friction have not been separated.

To isolate the effects of ϕ on viscosity, we estimate $\eta(\phi)$ as the viscosity in the high-shear limit that is independent of $\dot{\gamma}$. In curves of $\eta(\phi)$ vs. $\dot{\gamma}$, this corresponds to the regime where $\eta(\phi)$ achieves a constant minimum value (Fig. 4, inset) and flow is approximately Newtonian (*43*). For each soil, $\eta(\phi)$ appears to increase rapidly with ϕ beyond a certain value (Fig. 4, inset); however, that value is different for each material. A generic result for dense suspensions is that viscosity diverges with the distance from jamming as $\eta(\phi) \propto (\Delta\phi)^{-2}$ (*43*). We estimate the jamming fraction for each of our soils by fitting a divergence relation to the viscosity measurements in the Newtonian regime (Fig. 4), where ϕ_m is a free parameter. The inferred jamming fractions vary over $0.47 \leq \phi_m \leq 0.57$ among our materials. However, data for all soil samples collapse onto a single curve of $\eta(\phi)$ vs. $\Delta\phi$ (Fig. 4a), indicating that these highly heteroge-

neous soils behave similarly to idealized suspensions once ϕ_m for each material is accounted for. Considering yield stress, τ_o varies from near zero for low-ϕ suspensions to approximately 200 Pa for the most dense suspensions considered in this study. We hypothesize that in the low-$\dot{\gamma}$ elastic regime, the yield stress also depends on the distance from jamming, $\tau_o \propto (\Delta\phi)^{-C}$, where C is unknown. Data confirm a strongly nonlinear relation with $C \approx 3$ (Fig. 4b) but also exhibit significant scatter, indicating that an additional factor is needed to explain the data. We return to this below.

We now have all the results in hand to test the proposed dimensionless constitutive relation given by Eq. (2). For all suspensions in which a reliable yield stress could be determined (see Methods), we nondimensionlize the flow curves (Fig. 3) such that $\tau^* = \tau/\tau_o$ and $\Gamma = \eta(\phi)\dot{\gamma}/\tau_o$, where $\eta(\phi)$ is determined by Eq. (3). The only undetermined variable is $\mu^c(\phi)$, the contact friction contribution. In principle this parameter is a complicated function of the static and dynamic friction coefficients, shear rate, and ϕ_m (*28*). Here we consider $\mu^c(\phi)$ a free parameter, however, and choose its value so that the inflection point in the dimensionless flow curves is centered on $\Gamma = 1$. The result is a collapse of all the flow curves, for different materials and volume fractions, onto a single dimensionless master curve (Fig. 5). The master curve is very well captured by Eq. (2). Moreover, the data are well fit by $N = 1$, indicating that the simplest rheologic model for the data is a Bingham plastic fluid.

Material controls on flow parameters

Three empirically determined parameters are sufficient to provide a complete first-order description of the flow curves for a given suspension of debris-flow materials: jamming fraction ϕ_m, yield stress τ_o, and contact friction $\mu^c(\phi)$. These parameters should be material properties that vary with the composition of each soil sample. The jamming fraction was determined from the high-$\dot{\gamma}$ regime where viscosity is independent of $\dot{\gamma}$, and where we expect the influence of

cohesion and aggregation to be negligible (*44*, *45*). The data verify that there is no relation between ϕ_m and sample mineralogy (Fig. S2). Variations in ϕ_m are correlated with sample polydispersity (Fig. 6a), a result anticipated from studies of idealized suspensions (*40*, *46*). In addition, ϕ_m generally decreases with increasing $\mu^c(\phi)$ (Fig. 5, inset) – consistent with previous findings that increasing particle friction reduces the jamming fraction (*32*, *33*) – though this effect is much weaker than that of polydispersity. We determined earlier that the first-order control on yield stress is the distance from jamming; hence, τ_o and ϕ_m are related. After controlling for this effect, there is weak evidence of a possible higher-order dependence of τ_o on clay content (Fig. 6). Finally, we find that values for ϕ_m are on average about 5% smaller than ϕ_{max}, the maximum possible packing fraction for each material (Fig. 6c). This maximum fraction was achieved by strongly centrifuging each sample (see Methods).

Discussion

Previous studies on the rheology of debris-flow slurries have reported widely varying degrees of shear thinning and even shear thickening (*9*, *10*, *12*, *16–20*), as determined by values for the flow index n from fitting the Herschel-Bulkley model (Eq. 1). We saw similar variation among our samples (Fig. 3). Traditional flow curves, that plot shear stress against shear rate, do not account for the effect of the jamming distance on suspension viscosity. Moreover, previous studies of debris-flow rheology did not determine the jamming fraction. Here we used the Boyer *et al.* (*28*) model to successfully describe the effect of jamming distance on viscosity for suspensions of debris-flow source materials. Then we employed a non-dimensionalization of the Herschel-Bulkley equation, first proposed by Coussot (*15*), to collapse all flow data onto a single master curve. Results indicate that rheology of debris-flow slurries is well approximated as a Bingham plastic fluid ($N = 1$ in Eq. 2), which suggests a straightforward physical interpretation of our data: flow is determined by the relative strength of the viscous stress compared to the yield

stress. For small Γ (large Bingham number) suspensions store stress elastically, and for large Γ they dissipate stress viscously. Apparent shear thinning (and sometimes shear thickening) arises in the transition from the former regime to the latter; *i.e.*, by increasing contributions of viscous dissipation as Γ increases. Physically, this indicates that the shear thinning regime represents gradual yielding, by progressive breaking of cohesive bonds with increasing Γ (*15*). This idea suggests that apparent variations in n, determined from fits to the Herschel-Bulkley relation, may be the result of sampling only a portion of the flow curve. For nearly jammed suspensions with large yield stresses, estimates of n are especially unreliable because stress varies little over the range of shear rates achievable in a rheometer. Although an additional stress associated with plastic dissipation at yield may be appropriate (*21*), the form of this term is not agreed upon (*47*, *48*) and its inclusion would not improve the fit to our debris-flow data.

It is important to point out the limitations of our findings in terms of their applicability to natural debris flows. Our experiments were conducted under constant volume conditions; this means that the effect of shear-induced "Reynolds" dilatancy, which is significant for free-surface granular flows like debris flows (*31*), was suppressed. On the other hand, the full suspension rheology model of Boyer et al. (*28*) includes this effect, which suggests a pathway for extending our results to free-surface conditions. Pore pressure evolution is known to be an important component in the stress balance that drives debris flows (*31*); a major limitation of steady-shear experiments like ours is that transient variations in pore pressure are neglected. Nevertheless, Eq. 2 may serve as a useful constitutive relation to be included in more sophisticated models (*31*), while recognizing that rheology alone is insufficent to model natural debris flows (*23*).

The most important finding of this study is how the rheology of debris-flow source materials is controlled predominantly by the distance from jamming, $\Delta\phi$. Debris-flows slurries with similar volume fractions may have very different viscosities and yield stresses; and materials with very different volume fractions may have very similar yield stresses and viscosities. This

means that determination of ϕ_m for debris-flow source materials is of the utmost importance for modeling the failure and mobility of debris flows in nature. Yet, to the best of our knowledge, no modeling studies have assessed site-specific values of ϕ_m for hillslope soils. Rather, an arbitrary reference value is usually chosen. Our results suggest that the jamming fraction is a meaningful material quantity that is mainly determined by the physical characteristics of particles; *i.e.*, grain size, shape, and roughness. Additionally, values for ϕ_m of our debris-flow source materials are on average 5% smaller than the maximum achievable packing fraction ϕ_{max} (Fig. 6c), in agreement with previous findings for idealized suspensions (*43*, *49*, *50*). This result makes sense because materials at ϕ_{max} must dilate in order to yield and flow. In this regard, ϕ_m is akin to the critical-state volume fraction in soil mechanics (*31*); it reflects how tightly packed grains are at failure for a given material. Yield stress is strongly related to ϕ_m and is hence controlled by physical characteristics (through friction). From previous work we expect that yield stress should also depend on the chemical composition of soil, in particular the concentration of clay (*8*, *15*), through its influence on cohesion. Our data hint that τ_o is also influenced by clay content for natural debris-flow source materials; however, any correlation is not convincing (Fig. 6b). The unexpectedly weak relation may be due to our inability to isolate true clay concentration using our methods, and/or the highly heterogeneous nature of the soils which include various other materials such as organics that were not characterized. The grain-scale origins of friction and cohesion in highly heterogenous natural soils deserve deeper scrutiny. From a practical perspective, this means that ϕ_m and τ_o must be determined empirically. Both quantities, however, can be readily obtained from standard rheometry techniques as described here.

The functional dependence of suspension viscosity and yield stress on the distance from jamming has several applications for natural geophysical flows. One use is in helping to categorize natural suspensions by their mechanical behaviors. For example, it has been suggested that

hyperconcentrated flows are differentiated from more-dense debris flows in that the former are Newtonian, while the latter are not (*35*). Our data indicate that yield stress becomes negligible and flows roughly Newtonian for $\Delta\phi > 0.2$, corresponding to a volume fraction that is less than half of the jamming fraction. This finding may help numerical modelers, who must choose the proper constitutive equation and corresponding solver for routing flows through channels. Our rheologic results may also help to understand the formation of debris flows by progressive bulking up, the inferred mechanism for the Montecito debris flows (*4*). Beginning with clear water ($\phi = 0$), viscosity first increases linearly with ϕ as sediment is entrained in the dilute regime (Eq. 3). The shear stress $\tau = [\rho_p\phi + \rho_w(1-\phi)]gHS$, where ρ_p and ρ_w are the respective densities of particles and water, also increases roughly linearly with ϕ. This means that the shear rate $\dot{\gamma} = \tau/\eta(\phi)$ would not change significantly as the flow progressively bulks up downslope. On approach to jamming, however, yield stress and viscosity diverge. The shear rate of the flow, $\dot{\gamma} = [\tau - \tau_o(\phi)]/\eta(\phi)$, would rapidly slow down as $\Delta\phi$ approaches zero. As the shear rate of the suspension slows, the soil entrainment rate would diminish (*51*).

The considerations above suggest a self-limiting behavior in the maximum ϕ that can be achieved by progressive bulking up on hillslopes. A previous field study estimated that soil erosion in the 2018 Montecito event created debris flows on the hillslopes, that achieved a volume fraction of $\phi = 0.51$ just before entering valley-bottom channels (*4*). This value sits right in the middle of the range of jamming fractions we determined from rheologic measurements of hillslope soils ($0.47 \leq \phi_m \leq 0.57$). This suggests to us that the Montecito debris flows were close to the jamming fraction. An independent estimate confirms this: the yield stress and viscosity of the Montecito debris flows, inferred from downstream observations, can only be reproduced in the laboratory under conditions that are very close to jammed ($\Delta\phi \sim 10^{-2}$; Fig. 4). This leads naturally to a question at the heart of the Montecito debris flows and similar post-wildfire debris flows: what was the role of burning in facilitating debris-flow initiation? There was no

systematic difference between burned and unburned soils in terms of grain size, mineralogy, jamming fraction and rheology. Burning is known to increase soil porosity and decrease effective cohesion, by removing subsurface biomass containing mostly plant roots (*52–54*). The study by ref. (*4*) indicates that fire-induced hydrophobicity of soil may have enhanced surface runoff by reducing infiltration of rainwater. We suggest that erosion was abetted by the loose state of burned topsoil – *i.e.*, the reduction in volume fraction and effective cohesion – which would make particles more easily entrained by overland flow. In the future, emerging techniques for rapid and sensitive *in-situ* characterization of soil erodibility (*55*) could be coupled with traditional geotechnical and hydrologic measurements to test and refine this idea.

References

1. N. R. Regmi, J. R. Giardino, E. V. McDonald, J. D. Vitek, in *Developments in Earth Surface Processes* (Elsevier, 2015), pp. 319–362.

2. P. Shen, L. Zhang, H. Chen, R. Fan, *Geoscientific Model Development* **11**, 2841–2856 (July 2018).

3. S. H. Cannon, E. R. Bigio, E. Mine, *Hydrological Processes* **15**, 3011–3023 (2001).

4. P. Alessio, T. Dunne, K. Morell, *Journal of Geophysical Research: Earth Surface* **126** (Nov. 2021).

5. J. Kean *et al.*, *Geosphere* **15**, 1140–1163 (June 2019).

6. T. Takahashi, *Annual Review of Fluid Mechanics* **13**, 57–77 (Jan. 1981).

7. X. Huang, M. H. García, *Journal of Fluid Mechanics* **374**, 305–333 (Nov. 1998).

8. C. Ancey, *Journal of Non-Newtonian Fluid Mechanics* **142**, 4–35 (Mar. 2007).

9. P. Coussot, *Mudflow rheology and dynamics* (A.A. Balkema, Rotterdam Brookfield, Vt, 1997), ISBN: 905410693X.

10. J. J. Major, T. C. Pierson, *Water Resources Research* **28**, 841–857 (Mar. 1992).

11. P. Coussot, J. M. Piau, *Rheologica Acta* **33**, 175–184 (1994).

12. L. Schippa, in *Granularity in Materials Science* (InTech, Oct. 2018).

13. S. W. Jeong, *Geosciences Journal* **14**, 359–369 (Dec. 2010).

14. B. Yu, Y. Ma, X. Qi, *Journal of Hydraulic Engineering* **139**, 364–373 (Apr. 2013).

15. P. Coussot, *Physical Review Letters* **74**, 3971–3974 (May 1995).

16. J. D. Parsons, K. X. Whipple, A. Simoni, *The Journal of Geology* **109**, 427–447 (July 2001).

17. C. J. Phillips, T. R. Davies, *Geomorphology* **4**, 101–110 (June 1991).

18. P. Coussot, M. Meunier, *Earth-Science Reviews* **40**, 209–227 (June 1996).

19. A. M. Pellegrino, L. Schippa, *Environmental Earth Sciences* **77** (Nov. 2018).

20. C. Xia, H. Tian, *Water* **14**, 1369 (Apr. 2022).

21. M. Caggioni, V. Trappe, P. T. Spicer, *Journal of Rheology* **64**, 413–422 (Mar. 2020).

22. R. M. Iverson, *Reviews of Geophysics* **35**, 245–296 (Aug. 1997).

23. R. M. Iverson, presented at the, vol. 1, 3rd International Conference on Debris-Flow Hazards Mitigation: Mechanics, Prediction, and Assessment, pp. 303–314.

24. R. M. Iverson, *Journal of Geophysical Research* **110** (2005).

25. D. L. George, R. M. Iverson, *Proceedings of the Royal Society A: Mathematical, Physical and Engineering Sciences* **470**, 20130820 (Oct. 2014).

26. K. R. Barnhart *et al.*, *Journal of Geophysical Research: Earth Surface* **126** (Dec. 2021).

27. D. Bonn, M. M. Denn, L. Berthier, T. Divoux, S. Manneville, *Reviews of Modern Physics* **89**, 035005 (Aug. 2017).

28. F. Boyer, É. Guazzelli, O. Pouliquen, *Physical Review Letters* **107**, 188301 (Oct. 2011).

29. A. J. Liu, S. R. Nagel, *Annual Review of Condensed Matter Physics* **1**, 347–369 (Aug. 2010).

30. É. Guazzelli, O. Pouliquen, *Journal of Fluid Mechanics* **852** (Aug. 2018).

31. R. M. Iverson, D. L. George, *Proceedings of the Royal Society A: Mathematical, Physical and Engineering Sciences* **470**, 20130819 (Oct. 2014).

32. F. Tapia, O. Pouliquen, É. Guazzelli, *Physical Review Fluids* **4**, 104302 (Oct. 2019).

33. M. A. Dafalla, *Advances in Materials Science and Engineering* **2013**, 1–8 (2013).

34. M. Hermes, M. Dijkstra, *EPL (Europhysics Letters)* **89**, 38005 (Feb. 2010).

35. T. C. Pierson, in *Debris-flow hazards and related phenomena* (Springer, 2005), pp. 159–202.

36. K. Morell, P. Alessio, T. Dunne, E. Keller, *Geophysical Research Letters*, e2021GL095549 (2021).

37. A. Remaître, J.-P. Malet, O. Maquaire, C. Ancey, J. Locat, *Earth Surface Processes and Landforms* **30**, 479–488 (Apr. 2005).

38. C. Besso, T. M. P. de Campos, *E3S Web of Conferences* **92**, ed. by A. Tarantino, E. Ibraim, 05002 (2019).

39. T. Bisantino, P. Fischer, F. Gentile, G. T. Liuzzi, presented at the WIT Transactions on Engineering Sciences.

40. A. Santos, S. B. Yuste, M. L. de Haro, G. Odriozola, V. Ogarko, *Physical Review E* **89**, 040302 (Apr. 2014).

41. S. Pednekar, J. Chun, J. F. Morris, *Journal of Rheology* **62**, 513–526 (Mar. 2018).

42. A. Puisto, M. Mohtaschemi, M. J. Alava, X. Illa, *Physical Review E* **91**, 042314 (Apr. 2015).

43. S. Pradeep, M. Nabizadeh, A. R. Jacob, S. Jamali, L. C. Hsiao, *Physical Review Letters* **127**, 158002 (Oct. 2021).

44. Y. Shan, X. Wang, J. Cui, H. Mo, Y. Li, *Journal of Marine Science and Engineering* **9**, 1216 (Nov. 2021).

45. J. Ramírez-Muñoz, G. Martínez-de-Jesús, A. Soria, A. Alonso, L. Torres, *Advanced Powder Technology* **27**, 1885–1897 (Sept. 2016).

46. K. W. Desmond, E. R. Weeks, *Physical Review E* **90**, 022204 (Aug. 2014).

47. E. Lerner, G. During, M. Wyart, *Proceedings of the National Academy of Sciences* **109**, 4798–4803 (Mar. 2012).

48. J. Lin, M. Wyart, *Physical Review E* **97**, 012603 (Jan. 2018).

49. E. Blanco *et al.*, *Proceedings of the National Academy of Sciences* **116**, 10303–10308 (May 2019).

50. B. Guy, M. Hermes, W. Poon, *Physical Review Letters* **115**, 088304 (Aug. 2015).

51. R. M. Iverson, C. Ouyang, *Reviews of Geophysics* **53**, 27–58 (2015).

52. M. B. Bodí *et al.*, *Earth-Science Reviews* **130**, 103–127 (Mar. 2014).

53. P. R. Robichaud *et al.*, *CATENA* **142**, 77–88 (July 2016).

54. V. N. Balfour, S. W. Woods, *CATENA* **111**, 9–24 (Dec. 2013).

55. F. Qian, D. Lee, G. Nikolich, D. Koditschek, D. Jerolmack, *Journal of Geophysical Research: Earth Surface* **124**, 1261–1280 (2019).

56. L. E. A. Harold P. Klug, *X-Ray Diffraction Procedures: For Polycrystalline and Amorphous Materials* (WILEY, May 1974), ISBN: 0471493694.

57. L. Poppe, V. Paskevich, J. Hathaway, D. Blackwood, *A laboratory manual for X-ray powder diffraction*, 2001.

58. C. R. Hubbard, R. L. Snyder, *Powder Diffraction* **3**, 74–77 (June 1988).

59. T. Y. Liu, D. W. Mead, D. S. Soong, M. C. Williams, *Rheologica Acta* **22**, 81–89 (Jan. 1983).

60. A. P. Shapiro, R. F. Probstein, *Phys. Rev. Lett.* **68**, 1422–1425 (9 Mar. 1992).

61. W. Nesse, *Introduction to Mineralogy* (Oxford University Press, New York, 2nd, 2012), ISBN: 0199827389.

Acknowledgments

Authors acknowledge the funding provided by: the Army Research Office (ARO, Grant W911NF2010113) and National Science Foundation (NSF) Materials Research Science and Engineering Center (NSF-DMR-1720530) to DJJ and PA; Petroleum Research Fund (ACS-PRF Grant 61536-ND8) and NSF National Robotics Initiative (NSF-NRI-INT Award 1734355) to DJJ; ARO (Grant W911NF-18-1-0379) to EM, and the John MacFarlane Foundation to TD. We would also like to acknowledge Dr. Siobhan Whadcoat, Dr. Andrew Gunn, Nakul Despande, and Bryan Maldonado for their support and additions to the project.

Materials and Methods

Grain Size

Grain size distributions for each sample were measured using a Beckman-Coulter Particle Size Analyzer LS13-320. Grain size was determined in 114 log-spaced bins over the range 0.04 μm to 2000 μm. Each sample was sieved at 0.5 mm, the lower limit of coarse sand; in every case the volume fraction of retained grains was small ($< 5\%$ of sample). All distributions contained two or three modes, and in many samples there appeared to be three distinct grain size populations.

Polydispersity

Polydispersity was measured following Santos *et al.* (*40*) as m_3/m_2^2 where $m_k \equiv M_k/{M_1}^k$, with M_k being the k^{th} moment of the size distribution. Statistical moments were determined by fitting a lognormal distribution to the grain-size data for each sample, using GraphPad Prism version 9.2.0 for Windows, GraphPad Software, San Diego, California USA, www.graphpad.com. The

software output includes what we refer to as the amplification factor A, standard deviation σ, and the mean μ. The individual moments for the size distributions are estimated as:

$$M_1 = (1/A)e^{(\mu+1/2\sigma^2)} \tag{4}$$

$$M_2 = (1/A)e^{(2(\mu+\sigma^2))} \tag{5}$$

$$M_3 = (1/A)e^{(3\mu+9/2\sigma^2)} \tag{6}$$

The regression analysis of the lognormal fits for the debris flow samples is available in the supplementary section S6.

Mineralogical Analysis

We utilized semi-quantitative X-ray Diffraction (XRD) measurements to infer mineralogical composition of each sample. Four main component percentages were determined for each sample: clay, quartz, mica, and feldspar. Qualitative and semi-quantitative information on the main mineral phases present in each sample was obtained using a Panalytical X'Pert X-Ray Diffractometer (XRD) (*56*, *57*). The system utilized cobalt Kα radiation set to 40 kV and 40 mA. Each sample was pulverized in its entirety with an agate mortar and pestle to manually pass through standard sieve number 325 (diameter < 44 μm) before being loaded into a 16 mm radius slide for analysis. The samples were scanned by the XRD for three hours at room temperature and relative humidity, using the quartz peak as a natural internal standard to calibrate for peak offsets from deviations in ideal Z height. The instrument operated from 5º to 80º 2θ with a step size of 0.017º 2θ over 4,412 steps. Mineral phases were identified using the Panalytical software program HighScore (*57*). Mathematical fits were used to determine the phases present along with the relative abundancies in each sample. HighScore's semi-quantitative reference intensity ratio (RIR) technique was used to determine the weight percentage of each mineral phase (*58*). Due to the chemical similarities between illite clay and mica minerals, these materials could not

be differentiated and were lumped together in our analysis. See supplementary section S3 for further information.

Rheometry

Rheological measurements were performed in a Bohlin Gemini model parallel plate rheometer, which provides a direct and sensitive measurement of viscosity with no prior calibration (*59*). All samples were prepared as slurries, a mixture of deionized water and sediment, and tested at $0.05 \leq \phi \leq 0.50$. The samples (5 mL) were inserted between two plates separated by a gap of 1 mm. While shear stresses as low as 10^{-2} Pa were recorded, stress estimates become unreliable at low magnitudes. A minimum reasonable value for stress can be estimated from the particle pressure associated with sedimentation, $\tau_{min} \sim \Delta\rho g a \approx 0.1$ Pa, where $\Delta\rho \approx 1600$ kg/m^3 is the density difference between particles and water and a = d/2 is the average particle radius (≈ 40 μm). Below this stress, particle sedimentation may be expected which would violate the assumption of uniform mixing within the sample volume. For our sample materials, this lower stress condition corresponds generally to suspensions with $\phi < 0.20$; accordingly, flow curves for these suspensions are not presented.

A standard protocol was established to ensure reproducibility and to probe hysteresis effects (*42*). After pre-shearing, each sample was sheared from a high shear rate, $\dot{\gamma}_{max} \approx 100\ s^{-1}$, to a low shear rate $\dot{\gamma}_{min} \approx 0.01\ s^{-1}$, in 14 equal steps with a hold time of 20 s at each $\dot{\gamma}$. The downward shear sweep ensured sample homogenization, memory removal, and aggregate break up. In the next step, samples were sheared from $\dot{\gamma}_{min}$ to $\dot{\gamma}_{max}$ with the same equilibration time (t = 20 s) at each $\dot{\gamma}$. The protocol of down-and-up shear sweep was performed twice for each sample. The corresponding τ values of the samples were recorded for each $\dot{\gamma}$ and averaged to produce a representative value for each $\dot{\gamma}$ point in a cycle. Given the presence of cohesive/attractive forces, there is a history dependence to the rheology due to the formation and

breakup of particle microstructures. At high $\dot{\gamma}$, shear forces overcome the cohesive/attractive forces, but as $\dot{\gamma}$ decreases we expect the aggregates to reform. The ramp cycles allowed us to average out the contribution of the hysteresis to the suspension stress and overall viscosity. Here, we consider only the averaged data at each $\dot{\gamma}$, and ignore the hysteresis and time-dependent effects which were found to be of second order.

Herschel-Bulkley Modeling

Data from rheometry measurements were modeled to determine the fit parameters, τ_o and n, for the Herschel-Bulkley model. Model fits were conducted through log-based transformation to calculate non-linear regressions of each data set with τ_o, n, and k all left as free parameters. Values of n ranged from 0.37-1.45. Values of τ_o ranged over approximately five orders of magnitude, from 10^{-2} Pa to greater than $> 10^2$ Pa. Values of τ_o less than 10^{-1} Pa were extrapolated from fits of some suspensions, but should be interpreted with caution given the estimated τ_{min} for our experiments.

Maximum Packing

Suspensions of soil samples were prepared by adding a known mass of hillslope material (m_p) to a known mass of deionized water ($m_{w,i}$) [i being initial], and mixing for 30 minutes. The maximum packing volume fraction for each soil suspension, ϕ_{max}, was obtained by centrifuging the suspension at 2100 rpm for 20 minutes. The stresses generated were on the order of 10^3 times the acceleration due to gravity g, which breaks the cohesive/attractive bonds between the particles and forces particles to settle to the bottom of the centrifuge tube forming maximum packed structures. By estimating the difference between the initial amount of water added to prepare the suspension ($m_{w,i}$) and the amount of supernatant water that was discarded after centrifugation ($m_{w,f}$), we estimated the respective ϕ_{max} values for each soil sample using the

equation:

$$\phi_{max} = \frac{(m_p/\rho_p)}{(m_p/\rho_p) + ((m_{w,i} - m_{w,f})/\rho_w)}. \tag{7}$$

Here, ρ_p and ρ_w are the densities of clay particles ($\approx$ 2600 kg/m^3) and deionized water (1000 kg/m^3), respectively.

Figures

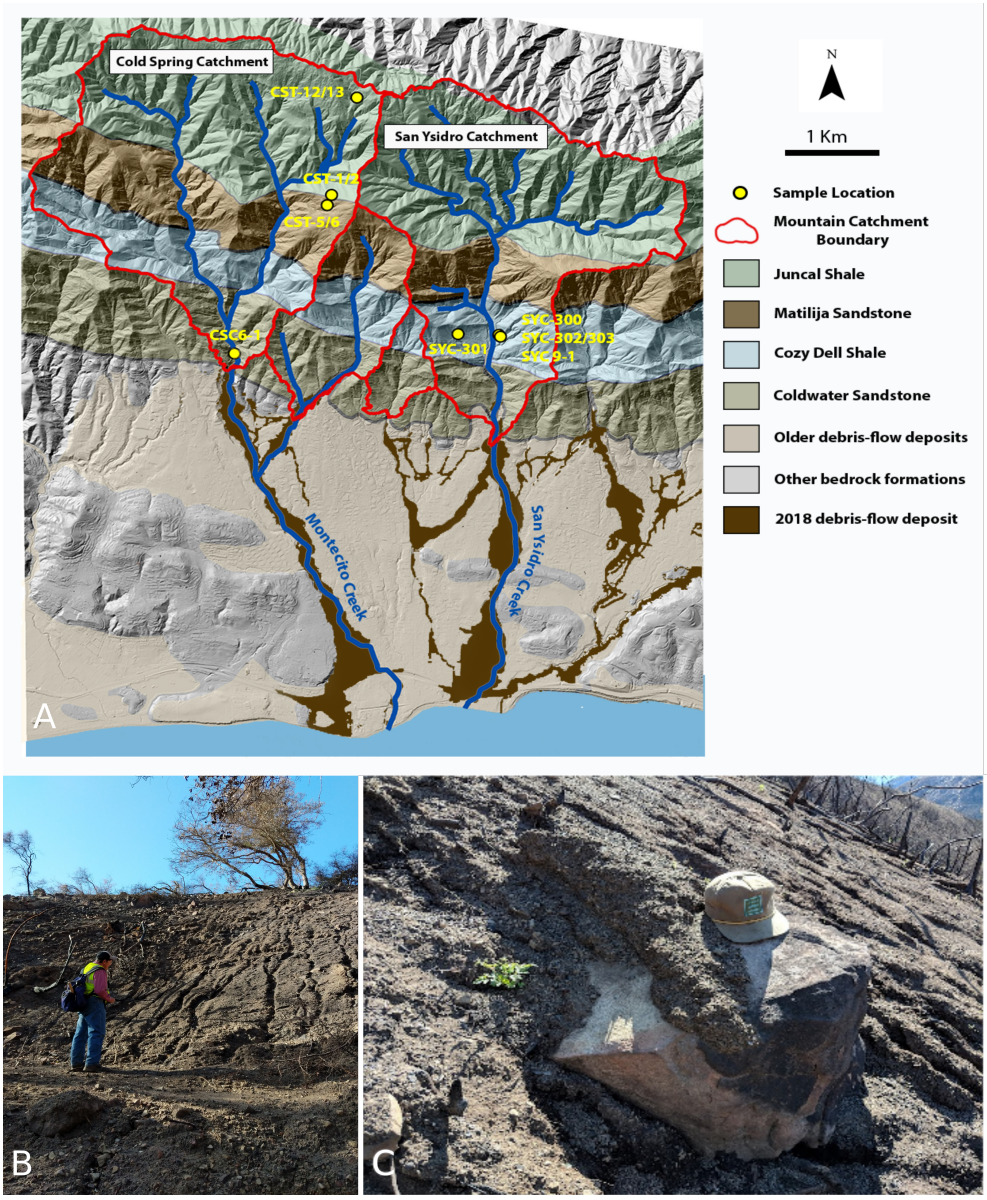

Figure 1: Field setting. (A) Digital Elevation Model of the Montecito region. Sample names used throughout this study are shown in yellow. Main catchment regions are designated in red, with the two primary catchments and fluvial channels of interest labeled. Major lithological units are shown throughout and denoted in the legend. Debris flow deposits from the 2018 event are indicated as a dark brown lithological unit with primary flow paths following the channel paths. (B) Field image showing a site of source material used for rheologic testing. Rills are the concentrated zones of erosion on the hillslope. (C) Close up of hillslope soil deposited on a boulder, showing that source materials formed viscous, yield stress flows.

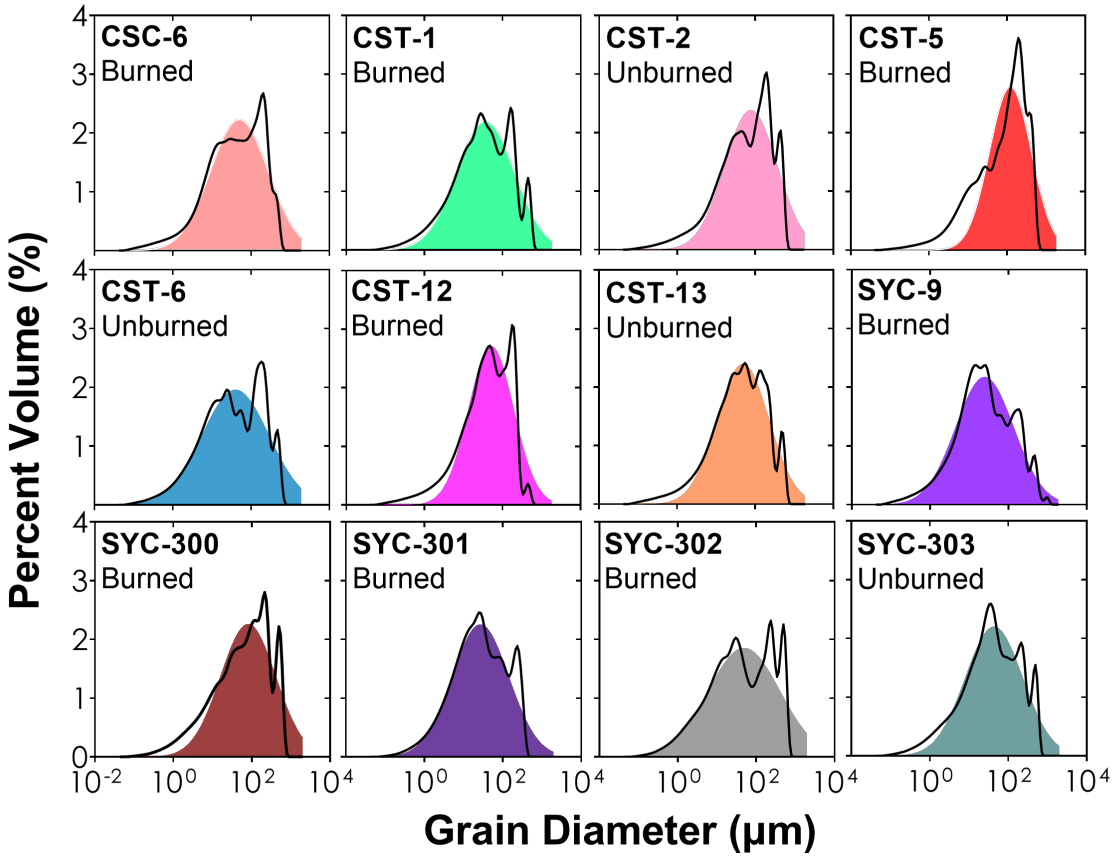

Figure 2: Grain-size distributions for all debris-flow source material samples; labels for each correspond to sample locations shown in Fig. 1A. Samples exhibit the most similarity in their content for grain sizes of silt and smaller ($< 60\,\mu$m). A strong peak in the fine sand range ($\sim 200\,\mu$m) is present for all samples. Most materials also display a peak in the coarse sand range ($\sim 500\,\mu$m) but this peak shows the greatest difference between samples. Log-normal distributions are shown that were fit in order to estimate the polydispersity for each sample, and color code for each sample is used for all figures.

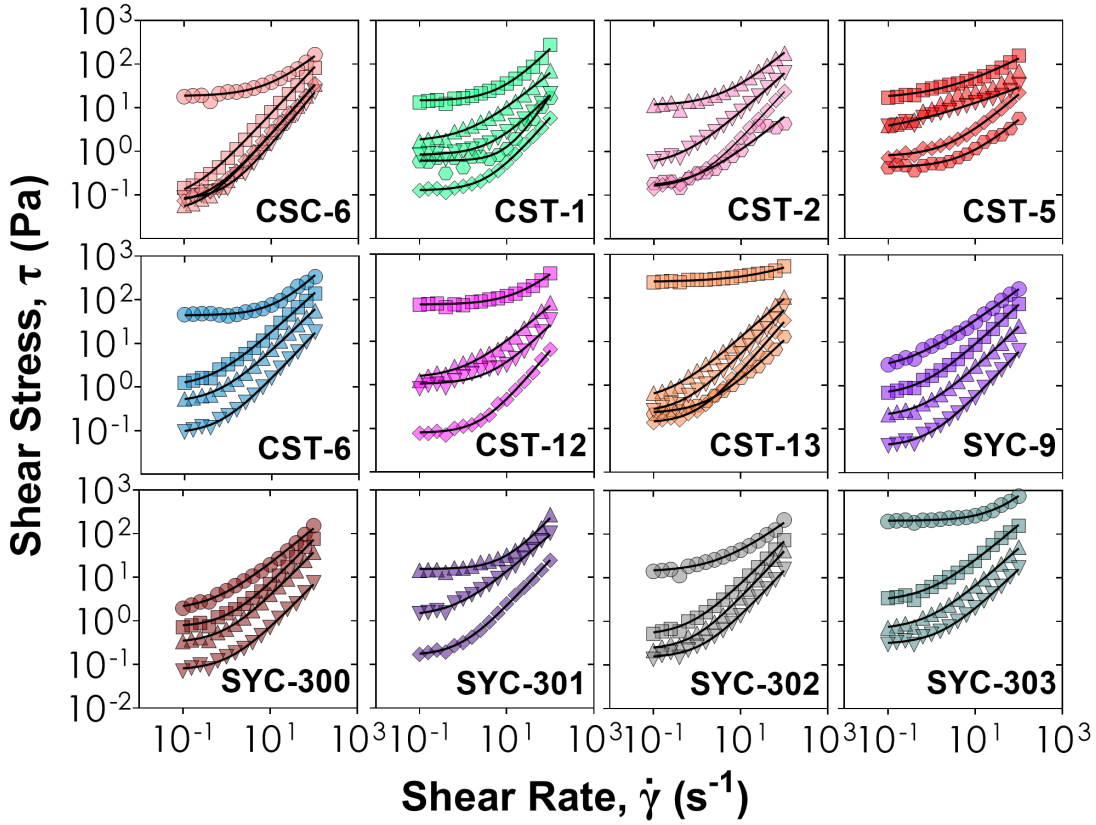

Figure 3: Shear-stress flow curves for various volume fractions (ϕ), for each soil sample analyzed. Only curves for which most measurements satisfy $\tau \geq 0.1$ Pa, the minimum reliable shear stress (see Methods), are shown here. Different ϕ values are indicated by their shape (circles: $\phi = 0.50$, squares: $\phi = 0.45$, upper triangles: $\phi = 0.40$, lower triangles: $\phi = 0.35$, diamond: $\phi = 0.30$, and hexagons: $\phi = 0.20$) while the different samples are color coded as in Figure 2. For all samples, shear stress increases by multiple orders of magnitude as the volume fraction increases from 0.20 to 0.50. Black lines show Herschel-Bulkley fits from Eq. (1) for each ϕ value.

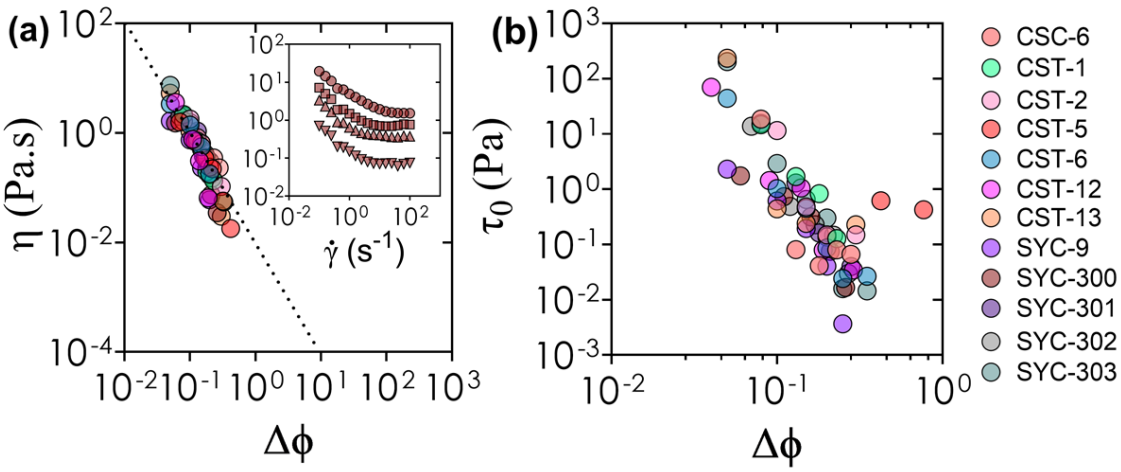

Figure 4: Rheology depends on the distance from jamming. Scaling of (a) viscosity (η) and (b) yield stress (τ_0) with the distance from jamming, $\Delta\phi = \phi_m - \phi$. The black dotted line in (a) shows the expected -2 scaling from the rheology of idealized dense suspensions (*28*). The inset shows viscosity data from an example material (SYC-300) for ϕ values of 0.50 (circles), 0.45 (squares), 0.40 (upper triangles), and 0.35 (lower triangles); note that viscosity decreases with shear rate but approaches a constant value in the high-shear limit. This limiting viscosity $\eta(\phi)$ was used to estimate the jamming fraction for each material, by fitting the equation $\eta(\phi) \propto \eta_f(\phi_m - \phi)^{-2}$ to the data. (b) Yield stress decreases rapidly with jamming distance, although scatter indicates another factor is necessary to explain the data. Note that all yield stress values determined from fits at all volume fractions are shown; however, values less than 0.1 Pa may be unreliable (see text).

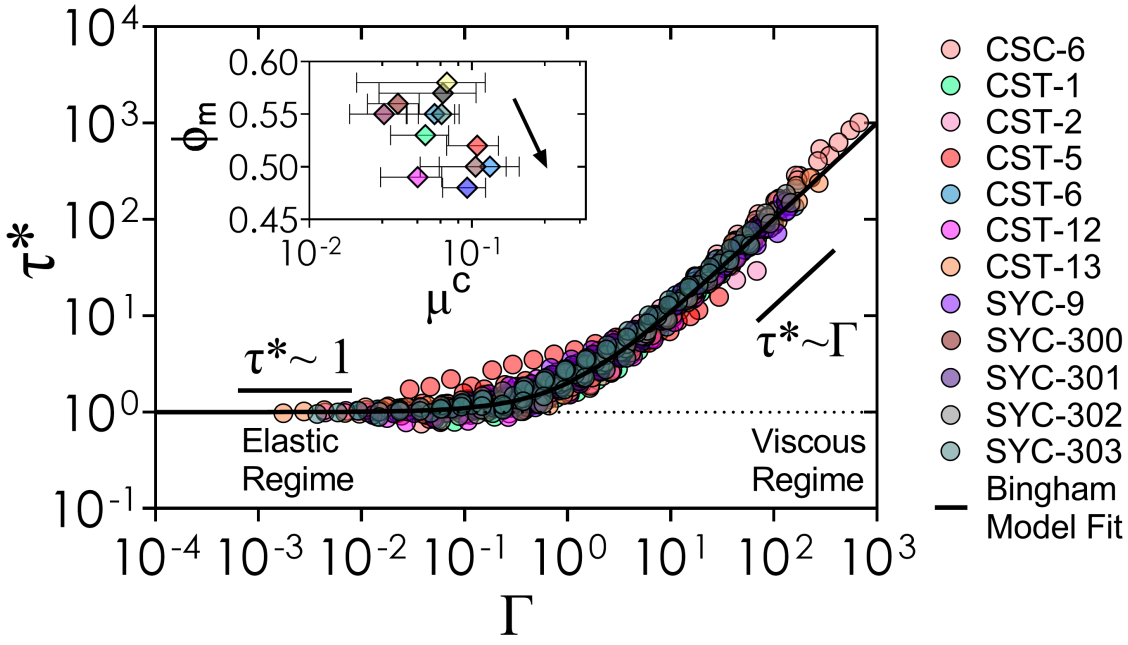

Figure 5: Non-dimensional master flow curve of $\tau^* = \tau/\tau_o$ vs. $\Gamma = \dot{\gamma}/(\tau_o/\eta(\phi))$, showing the collapse of the flow curves for all soil samples at all volume fractions. Two regimes are apparent: a low Γ regime exhibiting elastic behavior ($\tau = \tau_o$), and a high Γ viscous regime ($\tau = \eta(\phi)\dot{\gamma}$). The black line is the equation $\tau^* = 1 + \Gamma$, showing that a dimensionless Bingham plastic model ($N = 1$ in Eq. 2) provides a good first-order description of the data. Inset: Jamming fraction decreases weakly with the fit-determined contact friction parameter, μ^c.

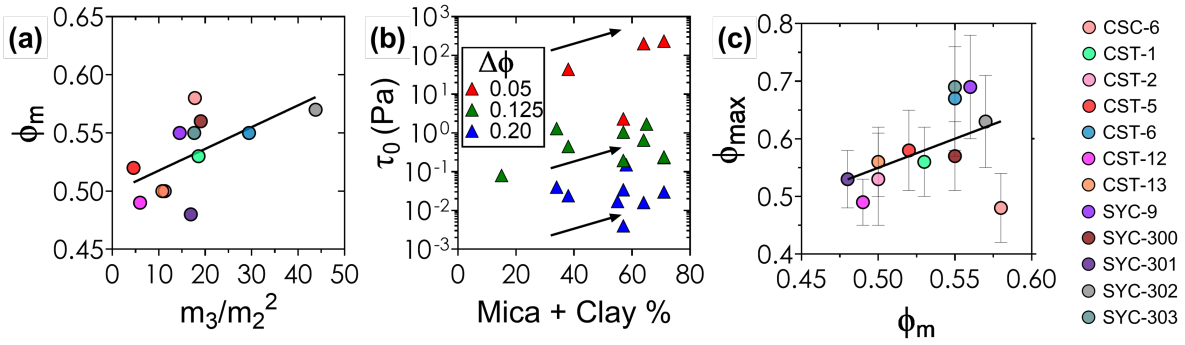

Figure 6: Material controls on flow parameters. (a) Jamming fraction (ϕ_m) linearly increases with the suspension polydispersity (m_3/m_2^2). Dark line indicates a linear fit to data with a slope of 0.0019 $\pm$ 0.0008 and y-intercept of 0.499 $\pm$ 0.016. (b) Yield stress (τ_0) may increase with Clay and Mica content (indicated by arrows) once the effect of distance from jamming is removed (indicated in legend); any relation, however, is weak. Note that all yield stress values determined from fits at all volume fractions are shown; however, values less than 0.1 Pa may be unreliable (see text). (c) Correlation between the jamming fraction ϕ_m determined from flow measurements, and the maximum packing fraction ϕ_{max} estimated from centrifugation. Line is a linear fit of the form $\phi_{max} = a\phi_m + b$ where $a \approx 1.01$ and $b \approx 0.05$. Note that one sample, CSC-6, has the un-physical result that $\phi_m > \phi_{max}$; this sample also showed a non-monotonic relation between viscosity and ϕ in the high shear-rate limit, which suggests that ϕ_m was poorly defined. Right-side legend indicates sample names for (a) and (c).

Supplementary Materials for
Rheology of debris-flow materials is controlled by the distance from jamming

Robert Kostynick[1,2†], Hadis Matinpour[3†], Shravan Pradeep[2†], Sarah Haber[4], Alban Sauret[3], Eckart Meiburg[3], Thomas Dunne[5], Paulo Arratia[6], and Douglas Jerolmack[2,6*]

[1]Washington University in St. Louis, Earth and Planetary Sciences, St. Louis, MO, United States
[2]University of Pennsylvania, Earth and Environmental Science, Philadelphia, PA, United States
[3]University of California Santa Barbara, Mechanical Engineering, Santa Barbara, CA, United States
[4]Ramboll US Consulting Inc., Princeton, NJ, United States
[5]University of California Santa Barbara, Bren School of Environmental Science and Management, Santa Barbara, CA, United States
[6]University of Pennsylvania, Mechanical Engineering and Applied Mechanics, Philadelphia, PA, United States

[*]To whom correspondence should be addressed; E-mail: sediment@sas.upenn.edu.
[†] Authors contributed equally to this paper.

[*]To whom correspondence should be addressed; E-mail: sediment@sas.upenn.edu.
[†]Authors contributed equally to this paper.

Supplementary Text

S1. Sample Descriptions

The debris-flow source materials examined here were collected from hillslopes burned by the December 2017 Thomas Fire in Montecito, Santa Barbara County, CA (USA). The samples were obtained from the Montecito hillslopes and down fan from February to April in 2018, closely following the January 9, 2018, debris-flow event. Samples were usually collected in pairs: a surface sample of the upper 4-5 cm of soil containing "burned" materials, and a subsurface sample collected 5-10 cm below the surface where soil was "unburned". The idea of these co-located pairs was to isolate the effect of burning on the physical, chemical, and rheological properties of the soil. Typical samples filled 0.5 to 1-gallon plastic bags. All the samples are related to the source materials of the slurries that mobilized boulders from stream channels to create the debris flows, *i.e.*, they were obtained from the burned hillslopes of the mountain where clear evidence of detachment by surface runoff was measured. The watersheds of Cold Spring Creek and San Ysidro Creek were of primary interest as they supplied the majority of the slurry material and caused boulders to become mobile by inundation into urban areas (*5*). All samples tested here are from these two primary mountain watersheds and were collected approximately at midslope locations. Both watersheds are underlain by sandstone and shale formations (see map in Alessio *et al.* (*4*)). Although sampling sites are nominally identified as one or the other of these rock formations, bands of the other lithology occur within each formation, and the soil weathered from them becomes mixed as it moves downslope to the sampled site. Therefore, samples consist of various mixtures of weathered minerals from both lithologies. The samples from Cold Spring Creek watershed are labeled CST or CSC and those from the San Ysidro Creek watershed are labeled SYC in Table S1.

S2. Grain Size Results

Grain sizes ranged from $10^{-1}\mu$m to $10^{3}\mu$m after wet sieving. Mean grain size and median grain size (D_{50}) measurements vary widely among the samples, but D_{50} tends to be lower for San Ysidro Creek samples (see Table S2). Differences in grain size do not appear to correspond to the associated lithology or position within a watershed, because the soil materials originate from sandstone and shale beds thus mixing in the process of downslope transport. For some sites, we observed a noticeable difference between the textures of "burned" and "unburned" samples, but these differences were not consistent across all sites. All grain size distributions could be reasonably well approximated by a unimodal log-normal distribution (see Section S6); polydispersity was quantified from the moments of the logarithmic grain size distribution (see Table S2). While this simplification misses important characteristics (*e.g.*, modal peaks) of the distributions, it allows us to compare our results to previous studies that examined the influence of polydispersity on rheology (*41*, *60*). Similarly to the mean and median values, we see no systematic difference in polydispersity as a function of lithology or burned/unburned

conditions.

S3. Mineralogical Results

Each sample was analyzed using X-Ray Diffraction (XRD) to determine four primary mineralogical components. The first component was quartz, with the chemical formula SiO_2. The second was clay minerals, *e.g.*, kaolinite or $Al_2Si_2O_5(OH)_4$. The third component was mica minerals, with a general formula of $X_2Y_{4-6}Z_8O_{20}(OH,F)_4$, where X is commonly Na, K, or Ca, Y is commonly Al, Mg, or Fe, and Z is either Si or Al. Illite, a clay mineral, has similar structure and composition to mica minerals (*61*) with X being primarily composed of K. Due to this similarity, apparent mica content could include possible cohesive material in the form of illite. The final component was feldspar, which has a variable formula depending on the cation present but holds a general formula of $XAl_aSi_bO_8$, where X is the cation Na, K, or Ca, *a* is either 1 or 2, and *b* is either 2 or 3. Figure S1 shows the compositional percentage of the samples in Table S1. Only quartz and clay minerals shared a correlation; quartz content decreased with increasing clay (or clay+mica) content.

S4. Jamming & Mineralogy

To examine possible material controls on the jamming fraction ϕ_m (the transition between rigid and flowing states of a suspension), each mineralogical component was compared to the value for ϕ_m of each sample (Fig. S2). There is perhaps a weak correlation with quartz content, and no correlation with any other mineral. Data indicate that ϕ_m does not depend significantly on the mineralogic composition of the soils.

S5. Regression Analysis of Polydispersity

Lognormal distributions were fit to raw grain-size data using the following equation:

$$Y = (A/X)e^{(-1/2(\ln(X/\mu)/\ln(\sigma))^2)}. \tag{8}$$

Here, X is the raw grain-size distribution, μ is the geometric mean, σ is the geometric standard deviation, and A is the amplification factor. The parameter A is related to the area under the curve and estimated using:

$$A = \mathrm{Area}/(\sqrt{2\pi}\ln(\sigma)). \tag{9}$$

The regression parameter R^2 is consistently high across all samples ($R^2 \geq 0.80$) and is independent of ϕ_m (Fig. S3). From these results we deduce that a lognormal distribution provides a first-order and unbiased fit to the grain-size data of all soil samples considered here.

Supplementary Figures

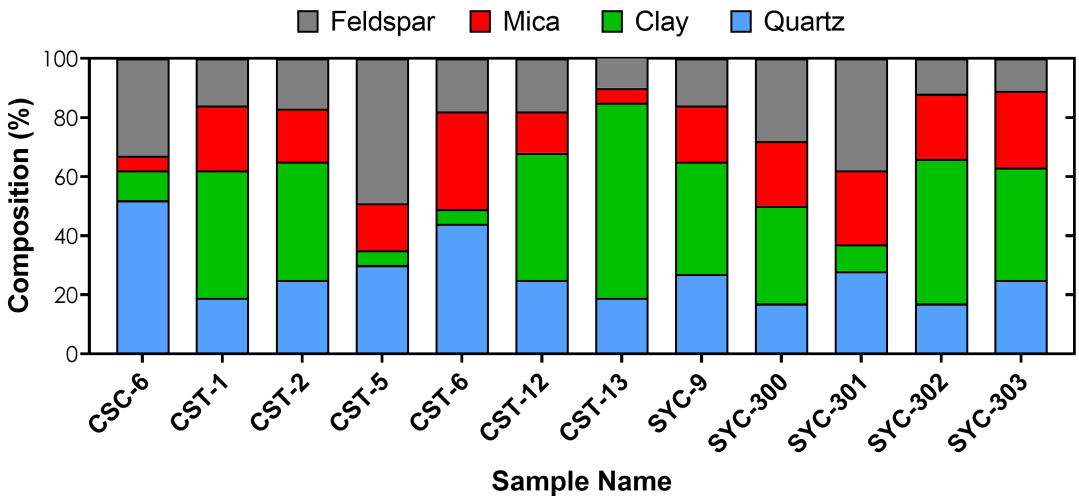

Figure S1: Distribution of mineralogical components present in each sample, measured using XRD. Blue, green, red, and gray bar graphs represent quartz, clay, mica, and feldspar, respectively. Quartz is the primary component of sample CSC-6 and CST-6. Clay is the primary component of CST-1, CST-2, CST-12, CST-13, SYC-9, SYC-300, SYC-302, and SYC-303. Feldspar is the primary component of CST-5 and SYC-301. Mica varies from sample to sample, but is always a minor component.

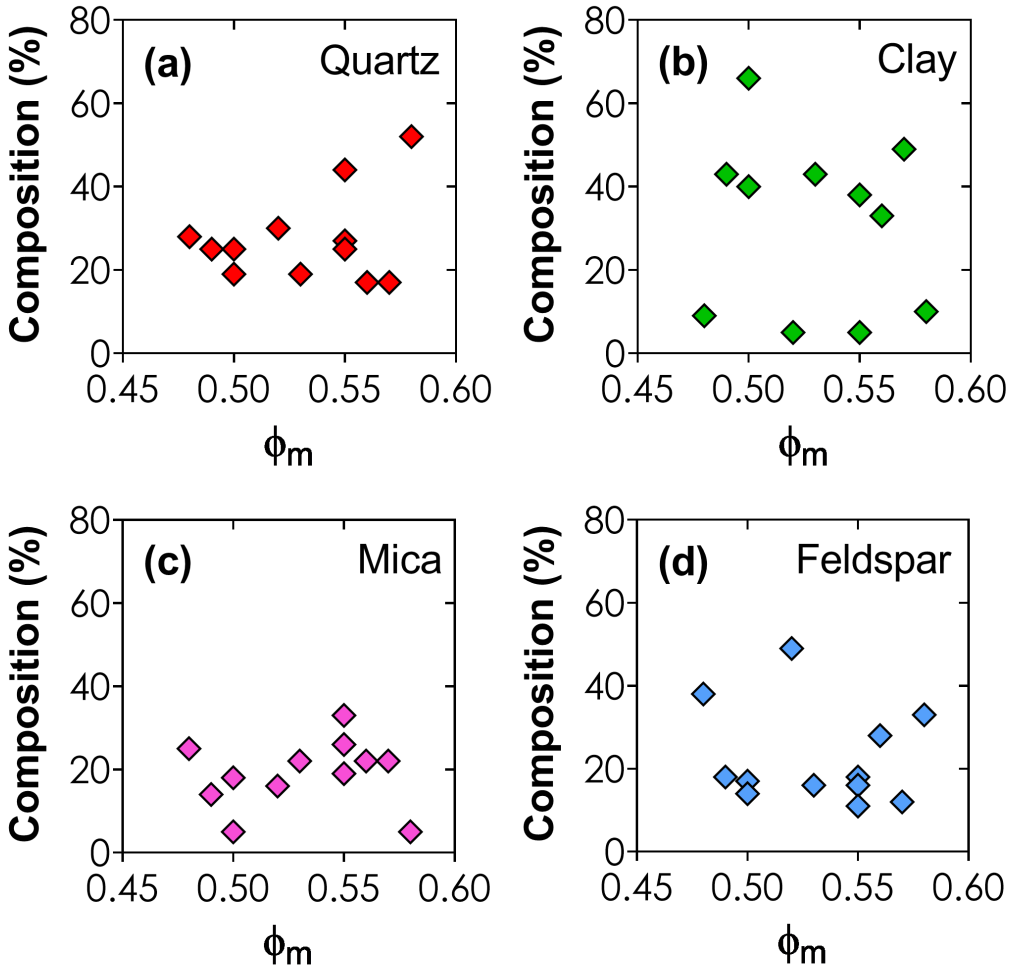

Figure S2: Comparison of mineralogy and the jamming fraction, ϕ_m. Plots (a)-(d) represent the percentage compositions of quartz, clay, mica, and feldspar, respectively. Results indicate no strong control of mineralogy on ϕ_m.

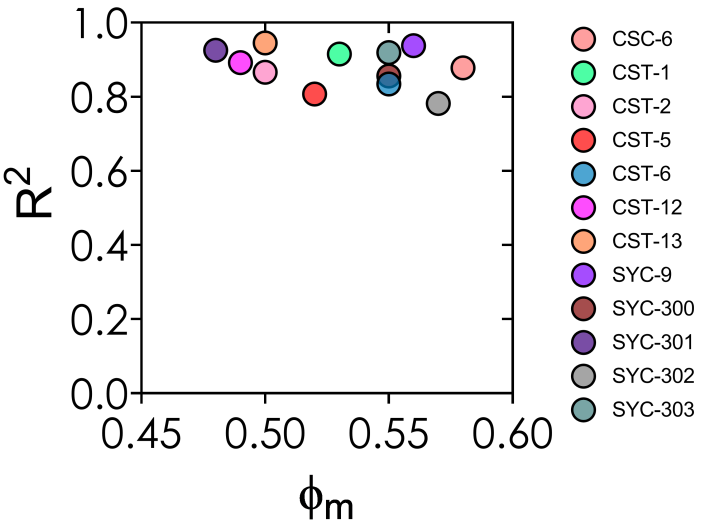

Figure S3: Regression coefficient R^2 for the lognormal fits for the particle-size distribution, as a function of the jamming fraction. Results indicate that lognormal distributions provide a good and unbiased fit to the data for all samples.

Supplementary Tables

Table S1: Descriptions of soil samples that were rheologically tested. Sample names are related to the location in which they were acquired (see Main Text Fig. 1). CST/CSC indicates samples acquired in the Montecito Creek Watershed. SYC indicates samples acquired in the San Ysidro Watershed. Gray shading indicates that the samples were obtained from the burned surface soils, while white shading indicates that samples were acquired from an unburned sublayer. A gold label indicates that the samples contain noticeable amounts of sandstone material cited by the field team, while black labelling indicates mixed material that contains significant amounts of shale material.

CSC-6	Overbank flow deposit. Small slide of burned material.
CST-1	Unrilled surface between rills. Upper 3 cm of blackened soil. Some coarsening of clast-rich surface.
CST-2	Brown-tan soil beneath blackened soil.
CST-5	Blackened surface layer of sandstone colluvium.
CST-6	Yellowish sandstone colluvium.
CST-12	Blackened surface layer with coarse surface layer (0.5 cm) removed.
CST-13	Yellowish tan subsoil layer.
SYC-9	Blackened surface layer on rilled hillslope. Colluvium.
SYC-300	Blackened surface layer on rilled hillslope. Upper 3 cm from ridge top.
SYC-301	Surface ash from upper 5 mm of topsoil.
SYC-302	Surface layer from upper 3 cm of topsoil. Blackened upper layer of rilled colluvium E tributary of SY Creek.
SYC-303	Unburned soil at 3-8 cm in sidewall of rill. E tributary of SY Creek.

Table S2: Mean grain size, median grain size (D_{50}) and polydispersity m_3/m_2^2 (see main text), determined from lognormal fits to each sample. Mean grain size has a range of $\sim$ 82 μm and the D_{50} has a similar range ($\sim$ 80.9 μm).

Sample Name	Mean (μm)	D_{50} (μm)	Polydispersity (m_3/m_2^2)
CSC-6	89.11	44.27	17.77
CST-1	81.85	34.61	18.57
CST-2	124.31	69.96	11.27
CST-5	139.85	104.52	4.57
CST-6	91.56	33.60	29.42
CST-12	76.53	46.07	5.98
CST-13	90.51	43.66	10.76
SYC-9	70.88	26.60	19.04
SYC-300	123.28	66.76	14.49
SYC-301	57.49	23.59	16.90
SYC-302	112.51	36.93	43.76
SYC-303	89.62	35.77	17.62